THESIS PROPOSAL

Title: Indirect measurement of proton cosmic-ray spectrum using gamma-ray data from Fermi Large Area Telescope

Student: Patomporn Payoungkhamdee 6138171 SCPY/M

Supervisor: Assistance Professor Warit Mitthumsiri

Degree: Master's degree

Field of study: Physics

Faculty of Science, Mahidol University

1 Introduction

Cosmic-ray research has been pioneered by Theodor Wulf who taked electrometer measured cosmic ray from the ground to higher altitude and much more experiment has confirmed that there is a cosmic ray from outer space which can penetrate and interect with the Earth atmosphere [1–3].

There are many possible phenomena of acceleration mechanism in the space that could produced high energy particles. Consequently, characteristic of acceleration machanism could roughly be distinguished by a spectral index in the arrival of cosmic ray spectrum in rigidity. Breaking point of the spectrum mainly come from the overlapped region of acceleration mechanism that could be an evidence to explore a new candidate of acceleration type.

In 2011, Pamela detecter indicate that there is a break point of proton cosmic ray spectrum around 240 GV [4]. Furthermore, AMS-02 also found a drastic change of proton CR spectrum at around 336 GV [5].

In this work, the indirect measurement of proton cosmic ray will be perform by using gamma-ray data from *Fermi* Large Area Telescope (*Fermi*-LAT).

2 Background knowledge

2.1 Cosmic rays

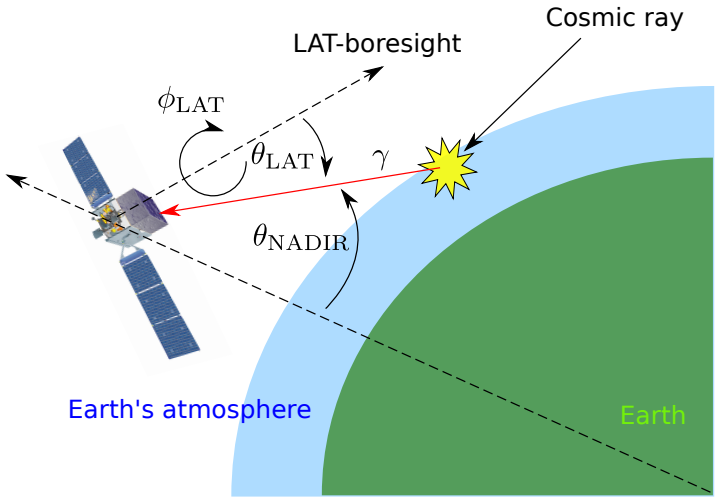

Figure 1: Schematics of γ-ray production

Cosmic rays are high energic particles which are produced in space by various types of acceleration mechanisms such as supernovae, active galactic nuclei, quasars, and gamma-ray bursts. The main composition of CRs consist of 90% protons, 8% alpha and other heavier atoms. The main reason that makes CRs spectrum follow power law function in rigidity is the acceleration mechanism was dominated in Lorenzian interaction which has a characeteristic spectral index.

CR spectrum has various spectral indices at different magnitude of energies, depending on the types of sources which can accelerate CRs to a certain energy range as shown in Figure 2 [6].

The motivation why we use γ-ray as a secondary product for investigate incident proton spectrum is that Earth limb's γ-ray relatively brigher than the sky due to collision from CRs in energy range 100 MeV and 1 TeV which consistent with our study [7].

Previous work has been performed using Pass 7 version data [8] and found an energy break point around 300 GeV with a significance of about 2σ [9]. This result is consistent with direct measurements from [4, 5].

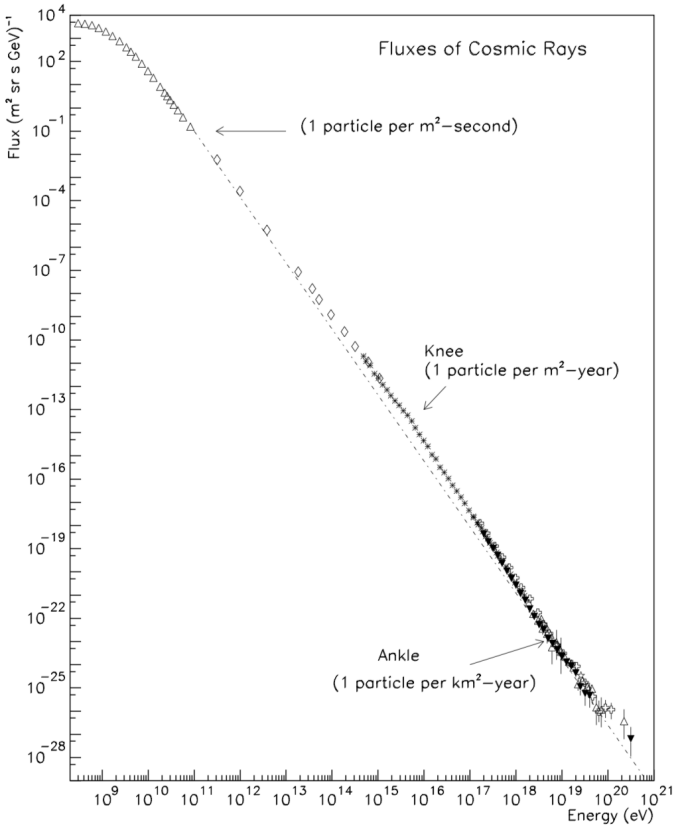

Figure 2: Main features of cosmic rays spectrum

2.2 *Fermi* Large Area Telescope

Gamma-ray Large Area Space Telescope (GLAST) could be informally called *Fermi*-LAT. The mission is to collect data of particles from multiple phenomena such as active galaxy nuclei (AGN), pulsars and other high energy sources. It also attach the Gamma-ray Burst Monitor (GBM) to study gamma-ray bursts. Fermi was launched on 11 June 2008 at 16:05 UTC aboard a Delta II 7920-H rocket.

Instrument

LAT consist with 16 layers of traker (TKR) modules, 16 calorimeter (CAL) and a parition ACD.

TKR module has made from an array of silicon-strip tracking detectors (SSDs) and has 18 tracker on a horizontal planes. First 12 planes have 0.035 radiation lengths, next 4 layes contain 0.18 radiation lengths thick and the rest of it does not have any converter. Tracking detector in each plane consist of two planar inner layer which running in x and y axis subsequently. The arrival γ-ray in LAT's field of view could produce electron-positron pair in TKR's plates. The initial lepton pair could be determined from the recoed of conversion point in SSD planes with a

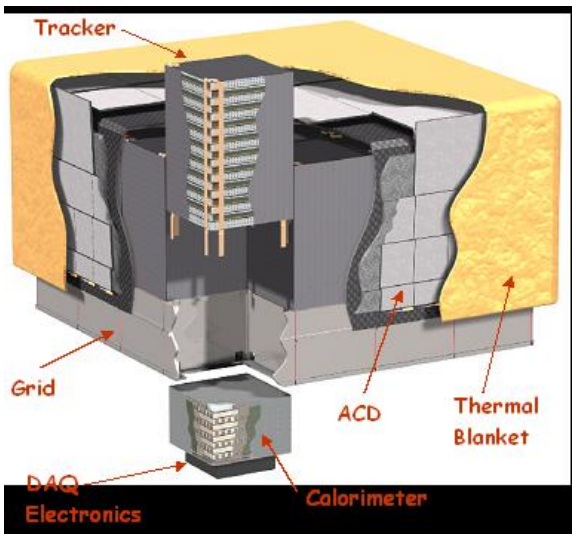

Figure 3: Instrument structure : Image taken from https://fermi.gsfc.nasa.gov

power angular resolution when has a low energy.

Each CAL module contains 1536 CsI(Tl) crystal with an 96 crystal align in eight different orthogonal layers. Dual PIN photodiodes also attach in each crystal which provide a great resolution in energy.

ACD tile contain wavelength shifting fiber by photomultiplier tubes (PMT) for redundancy. The tiles also are piled up in one direction.

Event reconstruction

The methodlogy of detection is to track the lepton pair product from an incident photon that collide with a conversion foils and lepton produc be traced by second inner layer of TKR. Consequently, the limit of precision depends on energy of photon that larger than mass energy of electron-positron as well as angle resolution of TKR that getting worser and worser at larger θ_{LAT}. Lastly, the lepton product could be measured the energy by a high precision crystal array in CAL. The event classification also divided into various level of confident event reconstruction with a different Instrument respondse function [10, 11].

3 Methodology and Scope

3.1 Data sets

Photon data with a newest version of events reconstruction (would be last version) from *Fermi*-LAT

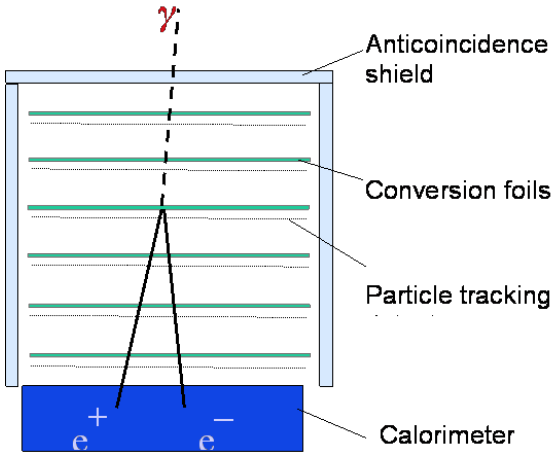

Figure 4: Schematic Structure of the LAT : Image taken from https://fermi.gsfc.nasa.gov

- P8R2_ULTRACLEANVETO_V6 data from 07/08/2008 to 16/10/2017 ($\sim$9 years)
- Collect photon energy range = 10 GeV to 1 TeV
- $\theta_{\mathrm{NADIR}} = 68.4° - 70°$(Earth's limb)
- Use $\theta_{\mathrm{LAT}} < 70°$

Note that the reasons that we use ULTRACLEANVETO type of event reconstruction are it is the cleanest reconstruction catalogue.

3.2 Flux extraction

1. Reprocess photon data by taking into account
   - Treat photon energy bias 3.7% that be affected the energy range above 10 GeV
   - Adjust limb angle due to LAT altitude shift due to detection of θ_{Limb} was tilt relatively to altitude of the spacecraft when orbit around asymmetric spherical Earth
2. Construct 2D histogram in Earth's angular coordinate (θ_{ZENITH} and ϕ_{EARTH})
3. Fill photon data in different energy range
4. Calculate exposure maps which include effctive area and time that LAT field of view can glimpse area of interest
5. Divide every single grid count map by exposure map

6. Sum over limb region of this map then divided by solidangle and energy bin width, then fill data in γ-ray energy spectrum as the formula 3.1

$$\text{Flux} \equiv \frac{dF}{dE} = \frac{\int_{\text{Limb region}}(\text{Count map/Exposure map})}{\Delta\Omega\Delta E} \tag{1}$$

7. Taking consider background subtraction from a average uniform background photon distribution by treating bin by bin

3.3 Coordinate Transformations

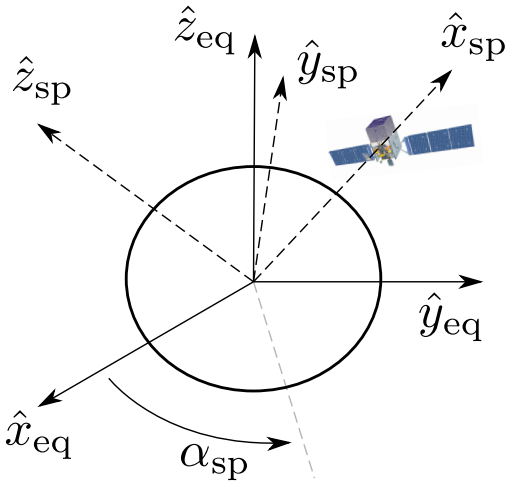

Figure 5: Coordinate transform between equatorial and spacecraft

$$\begin{aligned}
\hat{x}_{\text{sp}} &= \cos\delta_{\text{sp}}\cos\alpha_{\text{sp}}\hat{x}_{\text{eq}} + \cos\delta_{\text{sp}}\sin\alpha_{\text{sp}}\hat{y}_{\text{eq}} + \sin\delta_{\text{sp}}\hat{z}_{\text{eq}} \\
\hat{z}_{\text{sp}} &= -\sin\delta_{\text{sp}}\hat{y}_{\text{eq}} + \cos\delta_{\text{sp}}\hat{z}_{\text{eq}} \\
\hat{y}_{\text{sp}} &= \hat{z}_{\text{sp}} \times \hat{x}_{\text{sp}}
\end{aligned} \tag{2}$$

The transform matrix between equatorial coordinate and spacecraft coordinate could be represent as a relation in Eq 2

$$\hat{r}_{\text{sp}} \equiv T_{\text{eq}\to\text{sp}}(\delta_{\text{sp}}, \alpha_{\text{sp}})\hat{r}_{\text{eq}} \tag{3}$$

$$\begin{aligned}
\hat{x}_{\text{p}} &= \cos\delta^{\text{x}}_{\text{p}}\cos\alpha^{\text{x}}_{\text{p}}\hat{x}_{\text{eq}} + \cos\delta^{\text{x}}_{\text{p}}\sin\alpha^{\text{x}}_{\text{p}}\hat{y}_{\text{eq}} + \sin\delta^{\text{x}}_{\text{sp}}\hat{z}_{\text{eq}} \\
\hat{z}_{\text{p}} &= \cos\delta^{\text{z}}_{\text{p}}\cos\alpha^{\text{z}}_{\text{p}}\hat{x}_{\text{eq}} + \cos\delta^{\text{z}}_{\text{p}}\sin\alpha^{\text{z}}_{\text{p}}\hat{y}_{\text{eq}} + \sin\delta^{\text{z}}_{\text{sp}}\hat{z}_{\text{eq}} \\
\hat{y}_{\text{p}} &= \hat{z}_{\text{p}} \times \hat{x}_{\text{p}}
\end{aligned} \tag{4}$$

According to Eq 4, the transformation matrix between LAT-boresight and equatorial coordinate could be derived from

$$\hat{r}_{\rm p} \equiv T_{\rm eq\to p}(\delta^{\rm x}_{\rm p}, \alpha^{\rm x}_{\rm p}, \delta^{\rm z}_{\rm p}, \alpha^{\rm z}_{\rm p})\hat{r}_{\rm eq} \tag{5}$$

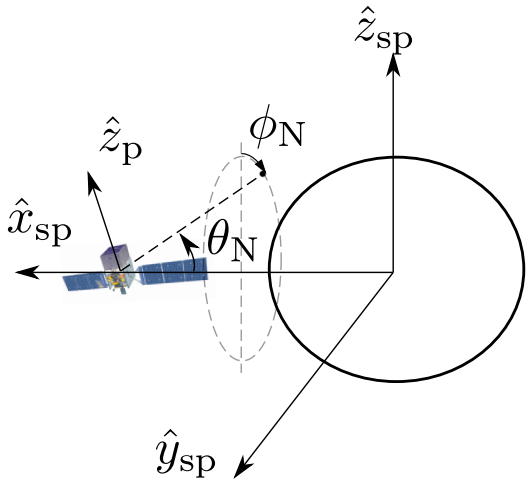

Figure 6: Coordinate transform between LAT-plane boresight and spacecraft

Importantly, the current status of lat field of view need to be consider in order to fill in the exposure map with the Earth's polar coordinate from satellite point of view as

$$\hat{r}^{\rm o}_{\rm sp}(\theta_{\rm N}, \phi_{\rm N}) \equiv -\cos\theta_{\rm N}\hat{x}_{\rm sp} + \sin\theta_{\rm N}\cos\phi_{\rm N}\hat{z}_{\rm sp} + \sin\theta_{\rm N}\sin\phi_{\rm N}\hat{y}_{\rm sp} \tag{6}$$

Since the spacecraft coordinate has already linked to the nadir's angle, the next step is to transform it into central coordinate which basically is the equatorial coordinate and convert it into LAT-boresight coordinate (Eq 7)

$$\hat{r}^{\rm o}_{\rm p}(\theta_{\rm N}, \phi_{\rm N}) = T_{\rm eq\to p}(\delta^{\rm x}_{\rm p}, \alpha^{\rm x}_{\rm p}, \delta^{\rm z}_{\rm p}, \alpha^{\rm z}_{\rm p})\left[T_{\rm eq\to sp}(\delta_{\rm sp}, \alpha_{\rm sp})\right]^{-1}\hat{r}^{\rm o}_{\rm sp}(\theta_{\rm N}, \phi_{\rm N}) \tag{7}$$

Geometrically, angular coordinate of LAT plane could be obtained from normalized component of the cartesian unit vector as in Fig 7. The exposure accumulation has been calculated in every single grid from the previous relation.

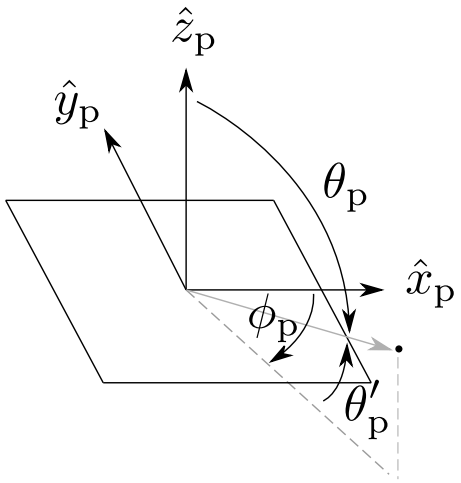

Figure 7: Detector's boresight in cartesian and polar coordinate

3.4 Interaction model

Trail incident proton spectrum in rigidity following relation

Single power law (SPL)

$$\frac{dN}{dR} = R_0 R^{-\gamma} \tag{8}$$

Broken power law (BPL)

$$\frac{dN}{dR} = \begin{cases} R_0 R^{-\gamma_1} \ : \ E < E_{\mathrm{Break}} \\ R_0 [R(E_{\mathrm{Break}})]^{\gamma_2 - \gamma_1} R^{-\gamma_2} \ : \ E \geq E_{\mathrm{Break}} \end{cases} \tag{9}$$

Note that power law spectrum in energy has shown in Appendix B.

In this work, we use the scattering amplitude from hadronic collision [12] that could produce a photon particle that could be detected by *Fermi*-LAT.

$$\frac{dN_\gamma}{dE_\gamma} \propto \int_{E_\gamma}^{E_{\max}} dE' \frac{dN_p}{dE'} \frac{d\sigma^{pp\to\gamma}(E', E_\gamma)}{dE_\gamma} \tag{10}$$

The atmospheric composition already known well enough that mostly combined with nitrogen gas as well as oxygen molecules [13]. In order to get scattering amplitude from proton-proton collision we treat a crossection of single hadronic collision with a fraction of nitrogen atom which is almost equal to oxygen atom [14] at relativistic level of kinetic energy.

In 2015, the direct measurement of Helium specrtum has been done by using AMS-02 in [15]. Improvement of model precision was included by taking into account incident of Helium cosmic ray particle as a first order correction and please

note that we ignore other heavier atom. The derived equation relation has shown in Eq 5

$$\frac{dN_\gamma}{dE} \propto \sum_{E_{\mathrm{inc,i}}} \left[\frac{E_{\mathrm{inc,i}}}{E_{\gamma,\mathrm{i}}}\Delta(E_{\mathrm{inc,i}})\right]\left[f_{pp}\frac{dN_{\mathrm{H}}}{dE_{\mathrm{inc,i}}}\left\{1+\frac{\sigma_{\mathrm{HeN}}}{\sigma pN}\left(\frac{dN_{\mathrm{H}}}{dR}\right)^{-1}\frac{dN_{\mathrm{He}}}{dR}\frac{dR_{\mathrm{He}}}{dR_{\mathrm{H}}}\right\}\right] \quad (11)$$

where

- Red color terms is using for incident proton spectrum that has form like Eq 3.4
- Use helium spectrum from AMS-02 measurement (2015)
- $f_{pp} \equiv E_\gamma(d\sigma^{ij\to\gamma}/dE_\gamma)$ is a table in K&O model which behave like a scattering amplitude that depend on the energy of incident particle
- Crossection $\sigma_{\mathrm{HeN}}/\sigma_{pN}$ at high energy (> 10GeV) is quite stable (≈ 1.6)

3.5 Optimization

Poisson likelihood function define as Eq 3.6

$$\mathcal{L} = \prod_{i=1}^{N} P_{\mathrm{pois}}(n_{\mathrm{i,model}}, n_{\mathrm{i,measurement}}) \quad (12)$$

Since our spectrum order is in different decade, we redefined a likelihood as a log-likelihood function for numerically reason like Eq 3.7. In addition,

$$Sum = \sum_{i=1}^{N} -\log P_{\mathrm{pois}}(n_{\mathrm{i,model}}, n_{\mathrm{i,measurement}}) \quad (13)$$

In order to get a best fit spectral indices, we do an optimization with a proper trial parameters for take gradient descent from Poisson loss function between model spectrum and flux from measurement as Figure 5

3.6 Monte Carlo Simulation

In this section, we perform a brute force method to find an error of any parameters (spectral indices and break point energy). For a **statistical error (random error)**, we rerandom a counts on each bin by poisson random generator and

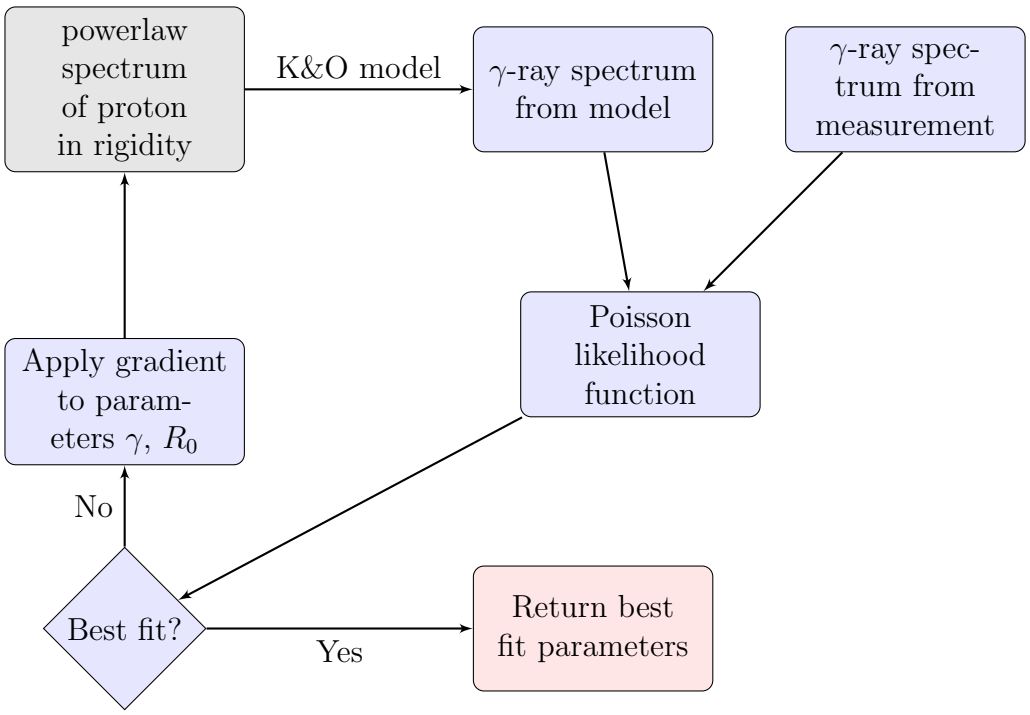

Figure 8: Flow chart of optimization process

recalculate the flux after that optimize it as the Fig 5 do. The process of this algorithm has shown in Fig 6. We do this process as much as gaussian distribution curve looks obvious enough which our work done is roughly 2000 sampling.

For **total error**, we also take into account erro from instrument which is LAT that depends on energy. We exactly the same as the statistical error determination but one more thing that including to this algorithm is to pick three energy bin (10, 100, 1000 GeV) then rerandom flux in these three bin and apply a cubic spline interpolation to smooth the line for a statistical reason [10]. The deminstration of this program is shown as Fig 7.

3.7 Likelihood ratio test (LRT)

In order to determine significant level between null model and alternative model, we use Wilk's theorem [16]. Basically, this method is to regard a given likelihood

$$\mathcal{L} \equiv \prod_{\alpha=1}^{n} f(x_\alpha, \theta_1, \theta_2, ..., \theta_h) \tag{14}$$

where

- x_α is represent a variant from model and data
- θ_i is a degree of freedom (DOF)

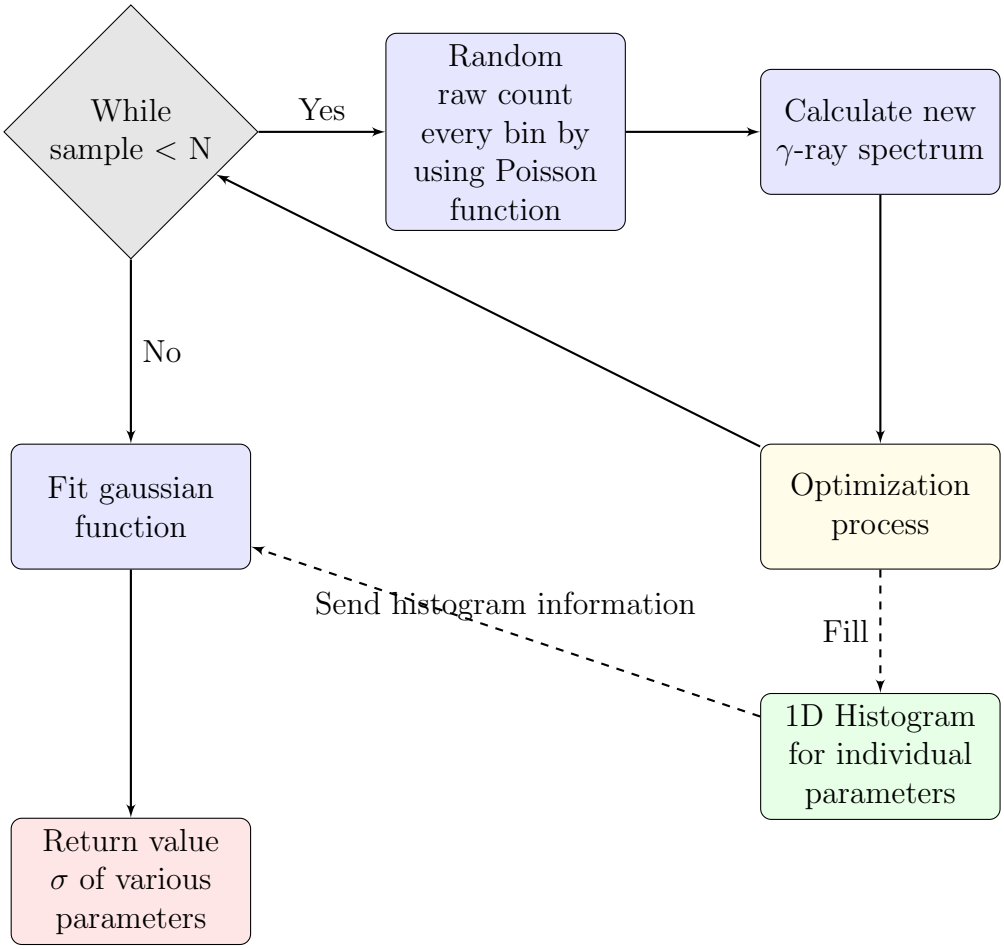

Figure 9: Flow chart of Monte Carlo simulation for statistical error

The explicit declaration with an obvious method to implement has been proved in [17] as the Equation 3.9

$$\mathrm{LRT} = -2\ln\left(\frac{\mathcal{L}_{\mathrm{null}}}{\mathcal{L}_{\mathrm{alternative}}}\right) \tag{15}$$

4 Research planning

References

[1] V. F. Hess (The Nobel Foundation, 1936).

[2] D. Pacini, Il Nuovo Cimento **3**, 93 (1912), URL `https://doi.org/10.1007/BF02957440`.

[3] J. Clay, Proceedings of the Section of Sciences, Koninklijke Akademie van Wetenschappen te Amsterdam **30**, 1115 (1927).

[4] O. Adriani, G. C. Barbarino, G. A. Bazilevskaya, R. Bellotti, M. Boezio, E. A. Bogomolov, M. Bongi, V. Bonvicini, S. Borisov, S. Bottai, et al., The Astrophysical Journal **765**, 91 (2013), URL http://stacks.iop.org/0004-637X/765/i=2/a=91.

[5] M. Aguilar (AMS Collaboration), Phys. Rev. Lett. **114**, 171103 (2015), URL https://link.aps.org/doi/10.1103/PhysRevLett.114.171103.

[6] S. Swordy, Space Science Reviews **99**, 85 (2001), ISSN 1572-9672, URL https://doi.org/10.1023/A:1013828611730.

[7] A. A. Abdo, M. Ackermann, M. Ajello, W. B. Atwood, L. Baldini, J. Ballet, G. Barbiellini, D. Bastieri, B. M. Baughman, K. Bechtol, et al. (Fermi-LAT Collaboration), Phys. Rev. D **80**, 122004 (2009), URL https://link.aps.org/doi/10.1103/PhysRevD.80.122004.

[8] M. Ackermann, M. Ajello, A. Albert, A. Allafort, W. B. Atwood, M. Axelsson, L. Baldini, J. Ballet, G. Barbiellini, D. Bastieri, et al., The Astrophysical Journal Supplement Series **203**, 4 (2012), URL http://stacks.iop.org/0067-0049/203/i=1/a=4.

[9] M. Ackermann, M. Ajello, A. Albert, A. Allafort, L. Baldini, G. Barbiellini, D. Bastieri, K. Bechtol, R. Bellazzini, R. D. Blandford, et al. (Fermi LAT Collaboration), Phys. Rev. Lett. **112**, 151103 (2014), URL https://link.aps.org/doi/10.1103/PhysRevLett.112.151103.

[10] M. Ackermann, M. Ajello, A. Albert, A. Allafort, W. B. Atwood, M. Axelsson, L. Baldini, J. Ballet, G. Barbiellini, D. Bastieri, et al., The Astrophysical Journal Supplement Series **203**, 4 (2012), URL http://stacks.iop.org/0067-0049/203/i=1/a=4.

[11] W. Atwood et al. (Fermi-LAT) (2013), 1303.3514, URL http://inspirehep.net/record/1223837/files/arXiv:1303.3514.pdf.

[12] M. Kachelrieß and S. Ostapchenko, Phys. Rev. D **86**, 043004 (2012), URL https://link.aps.org/doi/10.1103/PhysRevD.86.043004.

[13] J. M. Wallace and P. V. Hobbs, *Atmospheric* (Science, 2006).

[14] T. W. Atwater and P. S. Freier, Phys. Rev. Lett. **56**, 1350 (1986), URL https://link.aps.org/doi/10.1103/PhysRevLett.56.1350.

[15] M. Aguilar, D. Aisa, B. Alpat, A. Alvino, G. Ambrosi, K. Andeen, L. Arruda, N. Attig, P. Azzarello, A. Bachlechner, et al. (AMS Collaboration), Phys. Rev. Lett. **115**, 211101 (2015), URL https://link.aps.org/doi/10.1103/PhysRevLett.115.211101.

[16] S. S. Wilks, Ann. Math. Statist. **9**, 60 (1938), URL https://doi.org/10.1214/aoms/1177732360.

[17] J. P. Huelsenbeck and K. A. Crandall, Annual Review of Ecology and Systematics **28**, 437 (1997), https://doi.org/10.1146/annurev.ecolsys.28.1.437, URL https://doi.org/10.1146/annurev.ecolsys.28.1.437.

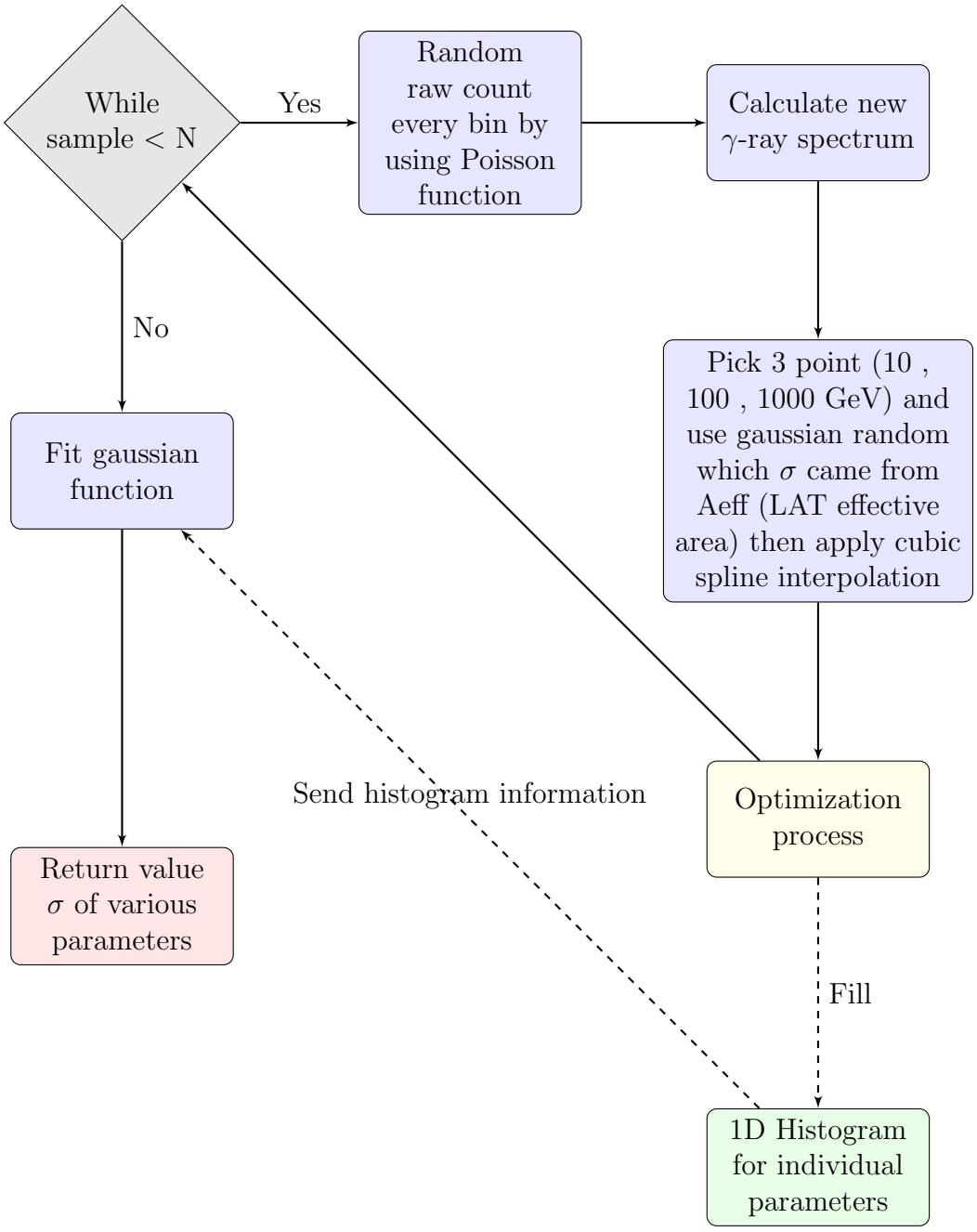

Figure 10: Flow chart of Monte Carlo simulation for total error